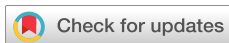


RESEARCH ARTICLE | MAY 15 2025

Scalable fabrication of single- and multi-layer planar lenses on fiber imaging probes

Fei He ; Rafael Fuentes-Domínguez ; Richard Cousins ; Christopher J. Mellor ;
Andrew Daniel Rocha ; Zuzana Adams ; Jennifer K. Barton ; George S. D. Gordon 



APL Photonics 10, 056114 (2025)
<https://doi.org/10.1063/5.0252562>



Articles You May Be Interested In

Two-scale structure of the current layer controlled by meandering motion during steady-state collisionless driven reconnection

Phys. Plasmas (July 2004)

15 May 2025 16:05:27



Your One-Stop Shop for the
Best Brands in Optics

- Extensive inventory with over 34.000 products available & 2.900 new products
 - Fast shipping from our 9 distribution centres around the globe
 - Bringing 80+ years of optical expertise to customers worldwide

 Edmund
optics | worldwide

[Shop Now](#)

Scalable fabrication of single- and multi-layer planar lenses on fiber imaging probes

Cite as: APL Photon. 10, 056114 (2025); doi: 10.1063/5.0252562

Submitted: 10 December 2024 • Accepted: 27 April 2025 •

Published Online: 15 May 2025



View Online



Export Citation



CrossMark

Fei He,^{1,a)} Rafael Fuentes-Domínguez,¹ Richard Cousins,² Christopher J. Mellor,³ Andrew Daniel Rocha,⁴ Zuzana Adams,⁴ Jennifer K. Barton,^{4,5} and George S. D. Gordon^{1,b)}

AFFILIATIONS

¹ Optics and Photonics Group, Faculty of Engineering, University of Nottingham, Nottingham NG7 2RD, United Kingdom

² Nanoscale and Microscale Research Centre, University of Nottingham, Nottingham NG7 2RD, United Kingdom

³ School of Physics and Astronomy, University of Nottingham, Nottingham NG7 2RD, United Kingdom

⁴ Wyant College of Optical Science, University of Arizona, Tucson, Arizona 85721, USA

⁵ Biomedical Engineering, University of Arizona, Tucson, Arizona 85721, USA

^{a)} Author to whom correspondence should be addressed: ezzfh2@nottingham.ac.uk

^{b)} Electronic mail: george.gordon@nottingham.ac.uk

ABSTRACT

We present a novel, scalable method for fabricating single- and multi-layer planar lenses on 125 μm -diameter fiber imaging probes, demonstrating preliminary capabilities for both lateral imaging (e.g., confocal microscopy) and axial imaging, using optical coherence tomography (OCT) as an exemplar. Hair-thin fiber endoscopes hold great promise for biomedical imaging, especially when paired with custom optics. For instance, OCT benefits from fiber facets that generate needle-like Bessel beams with a large depth-of-field (DOF), while wide-field imaging requires shorter DOF and higher lateral resolution. Current devices often rely on direct fabrication on fiber tips, which is incompatible with high-volume planar nano-fabrication necessary for producing low-cost disposable biomedical devices. In this paper, we propose a scalable fabrication approach compatible with semiconductor manufacturing, which also allows for simultaneous transfer of multiple devices onto fibers. We demonstrate this by transferring four planar lenses at once. To prove their imaging abilities, we designed and transferred a Fresnel zone plate, optimized for lateral imaging, and a diffractive axicon, optimized for axial imaging, onto fiber facets. The axicon fiber generates a needle-like Bessel beam with a 350 μm focal depth, retrieving focused images from a standard resolution target over a 150 μm range. We also present a preliminary demonstration of OCT imaging of reflective targets with a commercial system. Finally, we show that this approach supports multi-layer devices, by fabricating a two-layer Fresnel zone plate fiber probe, which exhibits good imaging performance. This method could enable the integration of complex, multi-functional optical structures onto fibers for advanced imaging and sensing applications.

© 2025 Author(s). All article content, except where otherwise noted, is licensed under a Creative Commons Attribution (CC BY) license (<https://creativecommons.org/licenses/by/4.0/>). <https://doi.org/10.1063/5.0252562>

15 May 2025 16:05:27

I. INTRODUCTION

Hair-thin fiber endoscopes are transforming biomedical imaging by enabling minimally invasive access with sub-cellular resolution, offering significant advantages for applications including high-resolution confocal microscopy,¹ *in vivo* bright-field, dark-field, and fluorescence microscopy in live brain tissue,^{2,3} quantitative phase and polarization imaging for early stage cancer detection,^{4,5} and optical coherence tomography (OCT) for imaging deep biological tissues.^{6–8} To meet the functional demands of these imaging

techniques, fiber endoscopes require on-tip light-shaping structures to manipulate light propagation. For instance, OCT applications benefit from enhanced depth of field (DOF), which often necessitates trade-offs between lateral and axial resolution.⁹ This can be addressed by generating needle-like Bessel beams, whose nearly uniform lateral spot size across an extended DOF allows for high-resolution tomography in deep tissues.^{10,11}

There are two main approaches to implementing such light-shaping functionality on fiber tips: direct fabrication and transfer processes. Direct fabrication approaches include techniques such

as focused-ion-beam (FIB) milling,^{12–15} chemical etching,^{16–18} and mechanical polishing,⁷ each offering precise control over optical characteristics. Similarly, 3D printing^{19–25} and nano-imprinting^{26,27} of photonic structures directly onto fiber tips have emerged as more flexible approaches for achieving complex light-shaping effects. For more compact designs, planar optics such as diffractive lenses^{25,27,28} and metasurfaces²⁹ can be engineered with sub-wavelength thicknesses using nano- and micro-scale structures. These planar systems allow precise spatial control over amplitude, phase, and polarization, delivering sub-wavelength resolution.^{30–33} However, despite their optical performance, these techniques face significant scalability challenges. Although 3D-printing and nano-imprinting have been increasingly demonstrating their potential for scalability in recent years,^{26,34} For the majority of the fabrication techniques mentioned earlier, their reliance on non-planar substrates limits compatibility with high-volume, wafer-centric lithographic techniques developed for the semiconductor industry, restricting their potential for widespread adoption.

Due to the limitations of direct fabrication on fibers, several techniques have been developed to transfer pre-fabricated optical patterns from planar substrates onto fiber facets.^{35–38} These transfer-based methods provide a promising route for implementing effective light-shaping elements onto fibers. However, recent advances have highlighted the need for great compatibility with multi-layer devices or metasurfaces,^{5,39} which can significantly enhance design flexibility and enable functionalities beyond what is possible with single-layer devices.^{40,41} Several studies^{42,43} have demonstrated the feasibility of using transfer approaches to stack multi-layered structures onto fibers. However, the nanostructures are directly stacked

on top of each other to enable a single functionality. Creating space between those stacked nanostructures would add a degree of freedom for different material use and/or functional design, allowing for more sophisticated control over phase, polarization, and other optical properties (e.g., one layer designed to focus light and the other to control polarization). In addition, their inability to scale up presents a challenge for high-volume production necessary for low-cost, disposable devices at commercial scale.

In this paper, we introduce a scalable alternative for fabricating planar lenses on fiber imaging probes, designed to be fully compatible with multi-layer devices and different imaging modalities. This process begins with high-resolution lithography on planar substrates [Fig. 1(a)] utilizing manufacturing techniques optimized for high-volume semiconductor production [Fig. 1(b)]. Following this, we utilize a key advantage of our method, the ability to transfer multiple devices simultaneously onto fiber substrates [Fig. 1(c)], significantly improving fabrication efficiency. Our approach employs conventional top-down nanofabrication techniques, including electron-beam lithography and lift-off processes, to define micro-scale planar lenses on bulk substrates. These lenses are then encapsulated in optically transparent polymers and released from the substrate by etching a sacrificial layer. The final step involves bonding the lenses to the fiber tips using adhesive, completing the transfer process in a manner compatible with multi-layer fabrication.

We demonstrate the scalability of our approach by simultaneously transferring four planar lenses onto fibers, a key milestone toward efficient, high-volume production processes. To illustrate the versatility of our method, we present two case studies: one for lateral imaging and another for axial imaging. In the lateral imaging

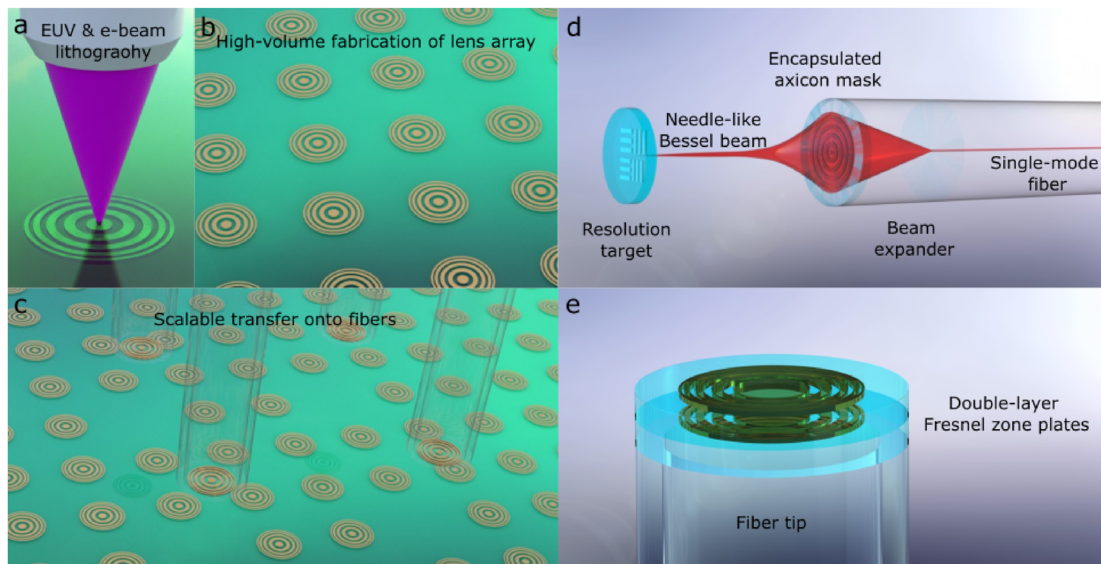


FIG. 1. (a)–(c) A scalable approach for high-volume fabrication of fiber endoscopic devices. The approach begins with (a) lithography on planar substrates compatible with (b) high-volume CMOS manufacturing processes and then enables the (c) simultaneous transfer of multiple devices onto fiber substrates. (d) and (e) Exemplar fiber devices fabricated via the approach. (d) An encapsulated axicon mask transfer-bonded onto a fiber facet (a piece of multi-mode fiber core as beam expander), which is capable of focusing light into a needle-like Bessel beam and imaging a resolution target over a large depth range. (e) The fabrication process is also capable of transferring multi-layer lens stacks, such as the two-layer Fresnel zone plates shown here, onto fiber tips.

case, we fabricate and transfer Fresnel zone plates onto fiber facets to generate Gaussian foci, while in the axial imaging case, diffractive axicons are used to shape light into Bessel-like beams [Fig. 1(d)]. We show that the axicon fiber generates a needle-like Bessel beam with a $350\text{ }\mu\text{m}$ focal depth. This beam maintains focused imaging of a USAF resolution target over a $150\text{ }\mu\text{m}$ range. We also show a preliminary demonstration of the compatibility of this device with a commercial OCT system via imaging reflective targets. In addition, we show the compatibility of our fabrication method with multi-layer designs by producing and characterizing a two-layer Fresnel zone plate structure on a fiber tip [Fig. 1(e)]. Notably, this two-layer fiber device produces high-quality images of a resolution target, highlighting the potential for future multi-functional devices, such as those enabling polarization control or achromatic focusing, to be implemented on fiber tips.^{5,40,41}

II. RESULTS

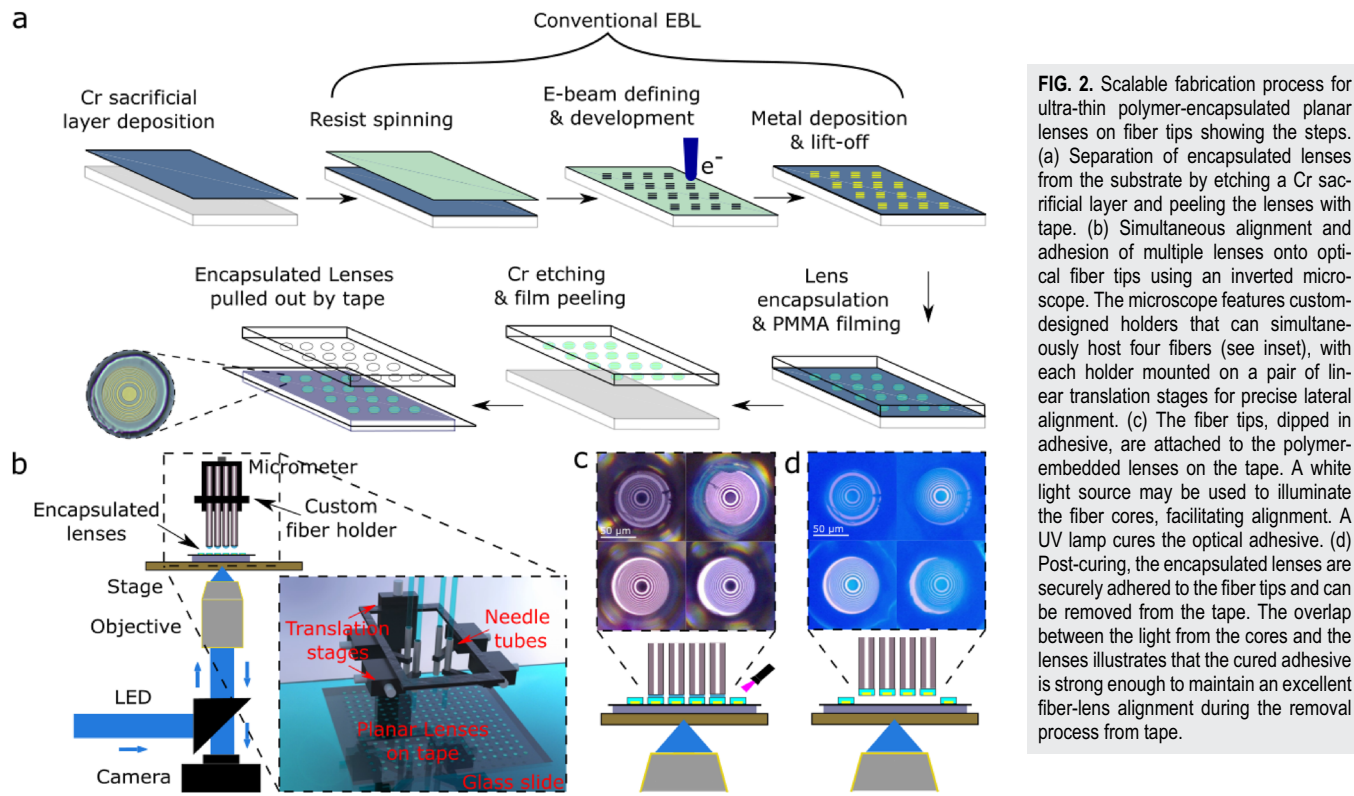
A. Scalable fabrication process

Our fabrication approach is summarized in Fig. 2. The first steps follow a standard EBL procedure for metallic structures on silicon substrates using a single-stage lift-off process. As shown in Fig. 2(a), a thin Cr sacrificial layer (5–10 nm) is deposited onto a silicon substrate, which is followed by spin-coating a positive tone e-beam resist (Allresist CSAR 6200.09), EBL, and development processes to create lens patterns in the resist layer. Thermal evaporation

is then used to deposit 100 nm Au (sufficient thickness for optical opacity), and the final lens patterns are defined by lift-off in AR 600-71. This widely adopted semiconductor-manufacturing compatible step is a key benefit of our technique that allows high-volume fabrication of high-quality planar micro- and nano-structures.

The next step is to spin-coat a 10–20 μm layer of OrmoClear resist (Micro Resist Technology) on top, align and pattern 125 μm disks (matching the fiber diameter) via maskless photolithography, thereby encapsulating the lenses in polymer. The functionalities of the OrmoClear encapsulation layer are to protect the lenses inside during the later transfer process and also to provide enough space between lenses within a multi-layered stack. The thickness of the encapsulation layer can be controlled by the spin-speed during the coating process. Next, a much thicker PMMA layer ($>500\text{ }\mu\text{m}$) is uniformly coated onto the Si substrate to assimilate the polymer-encapsulated lenses. The Cr sacrificial layer is then dissolved via a wet etch process in a commercial chromium etchant, which releases the PMMA film with the gold pattern lenses. The PMMA film here is used to hold those OrmoClear-encapsulated lenses, preventing them from dispersing in a liquid environment during the Cr etching process. The polymer disks are then peeled away from the PMMA film using weakly adhesive tape on the lens-facing side. The tape containing the polymer disks is then fixed (via taping the edges) onto a glass cover slip, which can be directly positioned onto the stage of a custom-built inverted optical microscope [as shown in Fig. 2(b)].

The inverted microscope allows imaging through the coverslip from underneath the stage in order to locate both lenses and fiber



tips within the field of view. The live image at the tape-lens plane is formed by a camera capturing the reflection, allowing the selection of good-quality lenses and visualization of fiber-lens alignment. The upper part of the inverted optical microscope, illustrated in the inset of Fig. 2(b), can simultaneously hold four fibers by custom-designed holders. Each holder consists of an arm fitted with a needle at its head, through which the fiber can be inserted. This setup allows the four fibers to be positioned closely during the transfer process.

The gap between the needle tube and the fiber provides flexibility for adjusting the fiber height. Each fiber holder is mounted on a pair of linear translation stages to assist with lateral alignment, and the vertical movement is provided by another translation stage hosting the four holders via a frame. During this process, white light is sent through the fibers to help visualize their core areas.

To adhere the polymer disks to the fibers, the fiber tips are first dipped in optical adhesive (Norland Optical Adhesive

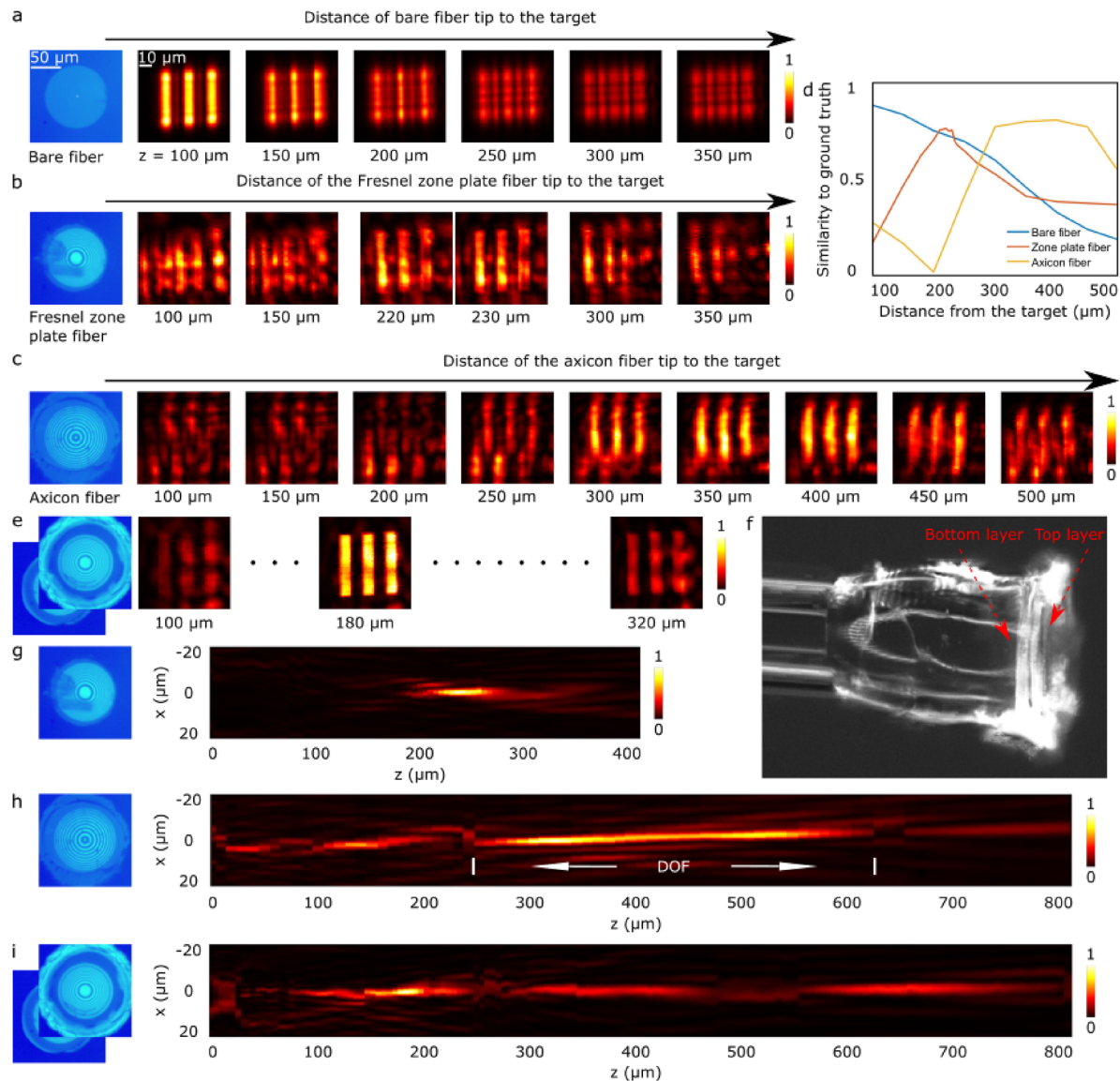


FIG. 3. Imaging performance of the fabricated fiber devices. (a)–(c) Images of the resolution target retrieved from (a) a bare fiber and the (b) zone plate and (c) axicon fibers at varying distances to the target. The images have identical sizes of $60 \mu\text{m} \times 60 \mu\text{m}$ in the x and y axes. (d) Similarities of the recorded images to the ground truth image at varying distances from 100 to 500 μm calculated via 2D-correlation. (e) and (f) Validation for the multi-layer compatibility of the fabrication approach by transferring and characterizing a two-layer zone plate fiber device. (e) Images of the resolution target retrieved from the device at the distances of $z = 100, 180$, and $320 \mu\text{m}$. (f) Microscope image of the two-layer device (side view). (g)–(i) The output beam profiles of (g) the zone plate fiber focusing light tightly, (e) the axicon fiber creating large-DOF Bessel beam, and (i) the two-layer zone plate fiber are depicted. The optical images of the lenses are shown on the left.

NOA 68). Then, they are aligned with encapsulated planar lenses and lowered until the fibers are in contact with the polymer surfaces, indicated by a small amount of excess adhesive spreading out from the tip. The adhesive is cured via UV exposure for 30–60 s [Fig. 2(c)]. Due to the strong bond formed between the polymer disks and the tips, the encapsulated lenses can be easily removed from the weakly adhesive tape by pulling the fibers up with the vertical micrometer. The images in Fig. 2(d) (Fresnel zone plates on multi-mode fibers) demonstrate excellent fiber-lens alignment maintained during the pulling process, as the light from the fiber cores (the white-bright area) overlaps well with the lens patterns. The transfer and adhesion processes are quick, typically taking only a few minutes to complete, and are highly repeatable with a low likelihood of failure, leading to suboptimal lens performance.

We analyzed 8 fabricated lenses (4 from Fig. 2 and the other 4 from Fig. 10) and found an average lens alignment standard deviation of $5.7 \mu\text{m}$, although we anticipate this could be improved to $1\text{--}2 \mu\text{m}$ given this is the accuracy of the micrometer. The level of precision is particularly advantageous when transferring a single device at a time, as it allows for more precise alignment control. Refining the fabrication process, including precision-engineered fiber holders and microscope automation, could eliminate the need for manual alignment between fibers and lenses. There are no fundamental barriers to scaling this approach further, as the highly regular grid of lenses naturally facilitates alignment, making it well-suited for mass production.

B. Experimental imaging performance

To demonstrate the versatility of our fabrication approach, we present two case studies involving the design and transfer of planar lenses with distinct focal properties: a Fresnel zone plate for a short-DOF Gaussian focus and a diffractive axicon for a large-DOF Bessel beam. While existing axicon fibers use 3D refractive structures,^{7,16–18,20} our 2D planar axicon offers a viable alternative with the key advantage of compatibility with high-volume semiconductor fabrication. Before the fiber-transfer step, the fibers are prepared with a small beam-expanding section to allow the beam to fill the aperture of the lens. This is fabricated by fusion splicing a piece of $105 \mu\text{m}$ -core multi-mode fiber (Thorlabs FG105LCA) onto a single-mode fiber (Thorlabs SM600) and then cleaving the endcap to the desired length of $750 \mu\text{m}$. The comparison between the output beam profiles from the Fresnel zone plate and axicon fibers is illustrated by Figs. 3(g) and 3(h) (measured via the optical setup in Fig. 5(a)). The Fresnel zone plate fiber has a tight focus at $235 \mu\text{m}$ with $100 \mu\text{m}$ DOF, while the axicon fiber creates a needle-like beam with $350 \mu\text{m}$ DOF for the main lobe. The design principles of the two fiber devices and their numerically simulated and experimentally measured point-spread-functions are illustrated in Figs. 6–8.

Next, we evaluate our two fiber devices in a resolution target imaging experiment. This shows the achievable imaging quality of the different designs and, therefore, their expected performance in imaging applications. In the context of endoscopic imaging, the ability of these devices to operate effectively at varying working distances is particularly important. The characterization of this is achieved via the setup described in Appendix A [Fig. 5(b)]. The scanned USAF resolution pattern has a width of $7.8 \mu\text{m}$ (64 pairs/mm, group 6 element 1). As illustrated in Fig. 3(a), a bare single-mode fiber

(Thorlabs SM600) is able to retrieve a high-fidelity image but only at small distances ($<100 \mu\text{m}$ from the target). However, the images become significantly blurred at $>150 \mu\text{m}$, and the main features of the pattern are unrecognizable after $200 \mu\text{m}$. Overall, the quality of the retrieved images drops dramatically as the fiber moves away from the target. This observation is quantitatively analyzed in Fig. 3(d) by the blue line—the correlation between a computer-generated ground-truth image and the fiber-retrieved images (correlation formula explained in Appendix B).

Despite the presence of some noise, the Fresnel zone plate fiber device is able to retrieve clear images (0.76 similarity) at a distance of around $230 \mu\text{m}$ [Fig. 3(b)], the device focal point, as indicated by the orange line in Fig. 3(d). Compared with bare fiber, the zone plate fiber has the advantage of retrieving a high-fidelity image at a distance that a bare fiber cannot, although with some additional artifacts that appear as background speckle. These artifacts may be due to the aberrated point-spread-function caused by fabrication imperfections on the lens, such as the shadow area in the left inset picture of Fig. 3(b). There may also be further artifacts arising from edge diffraction on the resolution target, though these could be reduced in future by using a less coherent light source such as an LED.

We note that the zone plate fiber device at its focal distance achieves imaging resolution comparable to a bare fiber at its facet. Based on the Rayleigh criterion, the device's FWHM spot size provides a $2.4 \mu\text{m}$ resolution (measured point-spread-function in Fig. 7), similar to the mode field radius of a single-mode fiber. With careful point-spread-function design, even higher resolution may be achievable. These devices can be designed to capture images over a wide range of distances, incurring a trade-off in resolution. The focal lengths range from a few micrometers (limited by ensuring ring sizes exceed the $20 \text{ nm EBL threshold}$) to the millimeter scale (limited by the number of rings that fit on a fiber facet).

The axicon fiber is able to retrieve clear images between 300 and $450 \mu\text{m}$ distances, as shown in Fig. 3(c). The yellow line in Fig. 3(d) shows that the similarity to the ground truth plateaus at $0.77\text{--}0.8$ over a $150 \mu\text{m}$ depth, 7.5 times longer than that of the zone plate fiber.

We also show the compatibility of our fabrication method with multi-layer structures by fabricating a two-layer Fresnel zone plate on a fiber, paving the way for ultra-thin, multi-modality fiber devices such as polarization converters or reflective beacons for fiber characterization,⁵ and metalens stacks for achromatic imaging.^{40,41} The device consists of two identical zone plate layers [a side view of the device is illustrated in Fig. 3(f)], fabricated by repeating the transfer and adhesion process [Figs. 2(b)–2(d)]. As shown in Fig. 3(e) (left inset), minor imperfections in the top layer, such as a missing ring and damage during detachment, may slightly affect the beam profile, contributing to discrepancies between experimental and simulated results (Fig. 9).

The three images in Fig. 3(e) are taken via the setup shown in Fig. 5(b) with the same resolution pattern and a $10\times$ objective (0.3 NA, $0.9 \mu\text{m}$ FWHM spot size in glass). These show that the device is able to retrieve a sharp image from the resolution target at the focal point $z = 180 \mu\text{m}$ [Fig. 3(i)], and the pattern can also be retrieved at two side focusing lobes ($z = 100$ and $320 \mu\text{m}$), albeit with compromised image contrast and quality. Due to the high losses of the double-layer diffractive lenses, a $10\times$ objective with an NA closer to that of the fiber device was used to improve light collection and

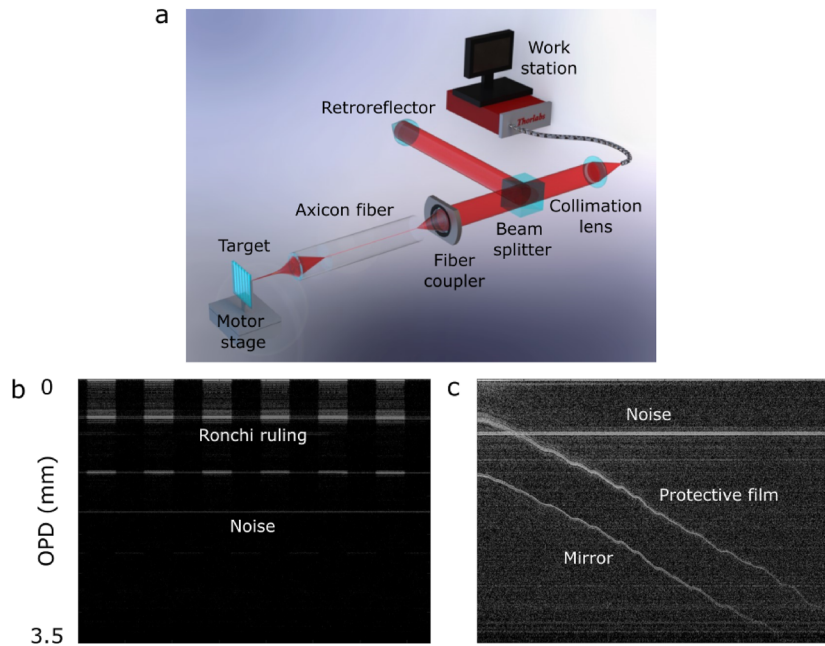


FIG. 4. OCT imaging test of the axicon fiber device. (a) A commercial OCT system is customized for our fiber-imaging setup—the test arm has a fiber coupler to focus collimated illumination into the axicon fiber. (b) OCT image of a Ronchi ruling laterally translated in front of the fiber tip. (c) OCT image of a reflective mirror translated axially from the fiber tip. The axial translation distance is shown by the optical path difference (OPD) between the test and reference arms.

ensure high-fidelity imaging. This also resulted in sharper images compared to the $20\times$ objective, due to reduced light divergence. The simulated photon efficiencies are 53.5% for the Fresnel zone plate fiber, 66.0% for the axicon fiber, and 40.6% for the two-layer Fresnel zone plate fiber.

Finally, we show a preliminary demonstration of the compatibility of the axicon fiber with OCT systems by imaging a Ronchi ruling (25 lp/inch) and a reflective mirror. A commercial OCT system (Thorlabs Telesto Series) is adapted for our fiber imaging setup, as illustrated in Fig. 4(a). The test arm has a fiber coupler (Thorlabs PAF2A-7B) to focus collimated illumination into the axicon fiber, which is trimmed to match the path length of the reference arm. The image of the Ronchi ruling [Fig. 4(b)] shows that the axicon fiber successfully resolves the grating pattern, producing alternating lines during lateral translation. The image of the reflective mirror [Fig. 4(c)] demonstrates that the fiber device can acquire a clear signal during its 3 mm axial translation (with a fixed reference arm path length). The noises come from autocorrelation artifacts, which arise due to backscattering or reflections from surfaces within the sample or optical components, resulting in spurious signals that can overlay the actual structural data. As the single-mode fiber used in our device is optimized for 660 nm, it is significantly mismatched with the OCT system used for testing, which operates at 1310 nm. This results in significant additional losses that can be reduced in the future iterations by using appropriate fibers such as SMF-28.

III. CONCLUSION

We have introduced a novel method for fabricating planar lenses on fiber imaging probes and demonstrated its scalability and compatibility with multi-layer devices and commercial OCT systems. This method is compatible with high-volume semiconductor

manufacturing processes and allows simultaneous transfer of multiple devices to fibers. We demonstrated the scalability by a simultaneous transfer of four Fresnel zone plates onto fibers. Although our approach utilizes optical adhesive, we did not observe any significant impact on the devices' performance. However, this method may be less suitable for fiber facets with micro-features (e.g., hollow-core fibers), as the adhesive could seep into the holes and affect the guided mode. Alternatively, a flexible membrane transfer that can wrap around the tip without adhesive can offer a more effective solution.⁴⁴

As an initial proof-of-concept demonstration of scalability, transferring four fibers in parallel is a reasonable starting point. However, our current transfer setup still requires individual alignment, but this could be solved in the future by automating the holder movement coupled with *in situ* feedback from a camera or power sensor. Furthermore, such alignment may only need to be performed on the first run since the spacing between lenses on the released substrate will remain the same across many samples. The fabrication process and fiber-transfer system can be further optimized and automated by precisely machining metallic holders for fiber arrays, ensuring that their spacing matches the pitch of the lens arrays on the substrate. This would enable simultaneous lens transfer onto a larger number of fibers while eliminating the need for individual lateral alignment. The estimated scalability is based on the dimensions of the lens array (e.g., 15 mm), the lens pitch (e.g., 300 μm), and the engineering constraints of the metallic holder (e.g., 1.2 mm spanning four lens pitches). Under these conditions, the calculated scalable number is 144, arranged in a 12×12 configuration. Therefore, this fabrication method holds considerable promise for mass production, significantly reducing the cost per fiber device.

In our case, the estimated marginal cost includes £4.60 for a bare fiber (priced per meter from Thorlabs) and ~£0.18 per planar lens (£900 to fabricate 5000 planar lenses, including all

necessary cleanroom steps at the University of Nottingham). While this estimate excludes fixed costs such as capital equipment and staff, it provides insight into the economies of scale achievable compared to commercially available individually machined fibers, which can cost between \$80 and \$160. The cost reduction is likely even greater when compared to the slowest and most expensive direct on-tip fabrication approaches, such as focused ion beam processing.

3D printing of micro- and nano-structures on fibers can take less than an hour⁴⁵ and cost less than \$100 per fiber device.²⁰ In our method, although the fiber-transfer step takes only a few minutes, the cleanroom fabrication steps (e.g., lithography and wet etching) typically require several hours, significantly increasing the time cost per device. However, as our fabrication process is compatible with e-beam lithography, it enables the creation of nanostructures smaller than 100 nm—beyond the typical 200 nm limit of 3D printing.⁴⁶ Those nano-structured features could also be fabricated by EUV lithography on planar substrates. Alternatively, they can even be fabricated by more widely available nano-imprint lithography—a desktop-based machine enabling a future large-scale process.

We note that previous studies^{26,38} have shown similar potential for scalability; our method provides an alternative that is also compatible with multi-layer devices. There is no theoretical limitation on the number of layers that can adhere, provided they remain sufficiently transparent to allow light transmission for alignment. To partially prove this, we successfully adhered five consecutive layers onto a piece of multi-mode fiber. We also note that the transfer process is not confined to highly specialized laboratories and can be performed in non-clean environments using low-cost equipment. In addition, the use of an optical microscope allows for easy selection of high-quality samples by testing their output fields before the transfer process, a form of in-process monitoring.

As a case study, we demonstrated that this fabrication process can produce designs potentially suitable for both lateral imaging (using confocal imaging as an exemplar) and axial imaging modalities (using OCT as an exemplar). We designed, fabricated, and transferred a Fresnel zone plate and a diffractive axicon onto fibers. While the zone plate produces a tight Gaussian focus, the axicon creates a needle-like Bessel beam with a 350 μm depth-of-field, showcasing the flexibility to tailor focal profiles for different applications. Resolution target tests revealed that the fiber devices retrieve good images from a standardized resolution pattern, despite minor aberrations. The axicon fiber, in particular, maintained image quality over a 150 μm range and performed OCT imaging on a Ronchi ruling and reflective mirror. The latter experiment shows preliminary compatibility of the axicon fiber with commercial OCT systems. Further optimization of the device for the OCT wavelength (e.g., using appropriate fiber such as SMF-28) could significantly enhance the performance for biomedical imaging. Gaussian optics can produce high quality needle like beams for OCT applications, as shown in existing works^{47,48} with performance comparable to or exceeding our diffractive axicons here. However, we emphasize the flexibility of our designs to produce both needle-like beams for axial imaging and highly focused beams for lateral imaging in a plane of interest. We also demonstrated that our fabrication approach produces multi-layer designs, which could

enable more complex multi-functional light-processing at the fiber tip. As proof-of-principle, we fabricated a two-layer Fresnel zone plate onto fibers and confirmed that the device has good imaging performance.

Binary amplitude masks shape light by blocking portions of the wavefront, which can introduce significant losses. In OCT experiments, they may suffer from reduced back-reflection efficiency due to absorption and scattering losses. This issue is more pronounced in multi-layered optics, where internal reflections can further degrade performance. A solution to these challenges is the use of discrete phase masks,^{11,49} which manipulate phase while preserving intensity, thereby improving transmission efficiency. Notably, lens-free and coded-aperture approaches have been shown to enhance imaging performance using binary amplitude masks in minimally invasive systems.⁵⁰ In addition, dielectric metasurfaces⁵¹ offer precise control over both amplitude and phase, potentially achieving higher efficiency than amplitude masks. To ensure compatibility with our approach, the materials used for discrete phase plates and dielectric metasurfaces must have a higher refractive index than the encapsulation layer, providing sufficient contrast with the surrounding environment for effective phase control, which remains a key challenge.

Notably, the polymer layer used in our approach has an independent thickness from the encapsulated structure. This layer not only provides mechanical protection to the structure during the transfer process, but also offers another degree of freedom to the structural design. For instance, these layers can be designed with different optical thicknesses, providing separations between functional layers. In addition, the encapsulated functional materials can be flexible, including many metallic and dielectric structures. Their combination may yield functionalities that are unachievable for a single-layer device, such as the works demonstrated by Avaya *et al.* and Zhou *et al.*^{40,41} By stacking triple-layer plasmonic and/or dielectric metasurfaces onto fibers, multi-wavelength achromatic foci can be achieved, desirable for many multi-spectral imaging applications. Owing to the good imaging performance of our fiber devices, we anticipate that these devices could be used as widely deployable endoscopic imaging devices such as fiber-OCT probes. They can be further expanded to designs such as spatiotemporal pulse-shaping axicons⁵² and super-oscillatory lenses generating sub-diffraction features.^{53–55} In addition, the compatibility of our approach to multi-layered designs could enable a new generation of multi-modality ultra-thin fiber-imaging devices, such as complex polarization state converters or reflective beacons for fiber characterization⁵ and metasurface stacks for achromatic fiber imaging.^{40,41} Finally, but more importantly, the scalability of the approach can enable low-cost disposable fiber endoscopic probes, facilitating widespread adoption.

ACKNOWLEDGMENTS

This work is supported by the UKRI Future Leaders Fellowship (Grant Nos. MR/T041951/1 and MR/Y034163/1). The authors would like to acknowledge the Nanoscale and Microscale Research Centre (nmRC) and School of Physics and Astronomy at the University of Nottingham for providing access to cleanroom facilities, and

the Wyant College of Optical Science at the University of Arizona for providing access to an OCT system.

AUTHOR DECLARATIONS

Conflict of Interest

The authors have no conflicts to disclose.

Author Contribution

F.H. performed the lens simulations, fabricated the fiber devices, conducted optical characterizations, and carried out the imaging experiments. Cleanroom fabrications were led by R.C. with additional help from F.H. USAF-target images were acquired by F.H. and R.F.-D. Z.A. set up the OCT instrumentation. F.H. and A.D.R. conducted the OCT measurements. G.S.D.G. led the original conceptualization of the fiber-device architecture and the overall experimental strategy. R.F.-D., C.J.M., J.K.B., and G.S.D.G. provided project supervision. F.H. drafted the manuscript, which was edited and approved by all authors.

Fei He: Formal analysis (lead); Investigation (lead); Methodology (lead); Visualization (lead); Writing – original draft (lead); Writing – review & editing (lead). **Rafael Fuentes-Domínguez:** Investigation (equal); Methodology (equal); Project administration (equal); Supervision (equal); Writing – review & editing (lead). **Richard Cousins:** Formal analysis (equal); Methodology (equal); Resources (lead); Writing – review & editing (equal). **Christopher J. Mellor:** Methodology (supporting); Resources (equal); Supervision (supporting); Writing – review & editing (equal). **Andrew Daniel Rocha:**

Formal analysis (supporting); Investigation (equal). **Zuzana Adams:** Methodology (supporting); Resources (equal). **Jennifer K. Barton:** Methodology (equal); Resources (equal); Supervision (supporting); Writing – review & editing (equal). **George S. D. Gordon:** Conceptualization (lead); Funding acquisition (lead); Methodology (equal); Project administration (lead); Resources (lead); Supervision (lead); Writing – review & editing (lead).

DATA AVAILABILITY

The data presented in this study are available from the following source: <https://doi.org/10.17639/nott.7547>.

APPENDIX A: EXPERIMENTAL CHARACTERIZATION SETUPS

To measure the output beam characteristics, the fiber devices are connected to a diode laser source (ThorLabs LPS-660-FC, 660 nm central wavelength), as illustrated in Fig. 5(a). A pair of lenses ($f_1 = 18$ mm and $f_2 = 250$ mm, giving a magnification of 13.9) is used to form magnified images of the focal spots onto a camera (XIMEA MQ042RG-CM). The depth-scan is performed by z-translation of the fiber devices with a motorized stage. The imaging performance is tested by illuminating resolution targets in a transmission-mode configuration and collecting light with the fiber devices [Fig. 5(b)]. An objective is used to focus a collimated light beam (from the 660 nm laser source) onto a standardized USAF resolution target (Thorlabs R1DS1N), which is collected through the fiber devices, which are connected in turn to an optical power meter

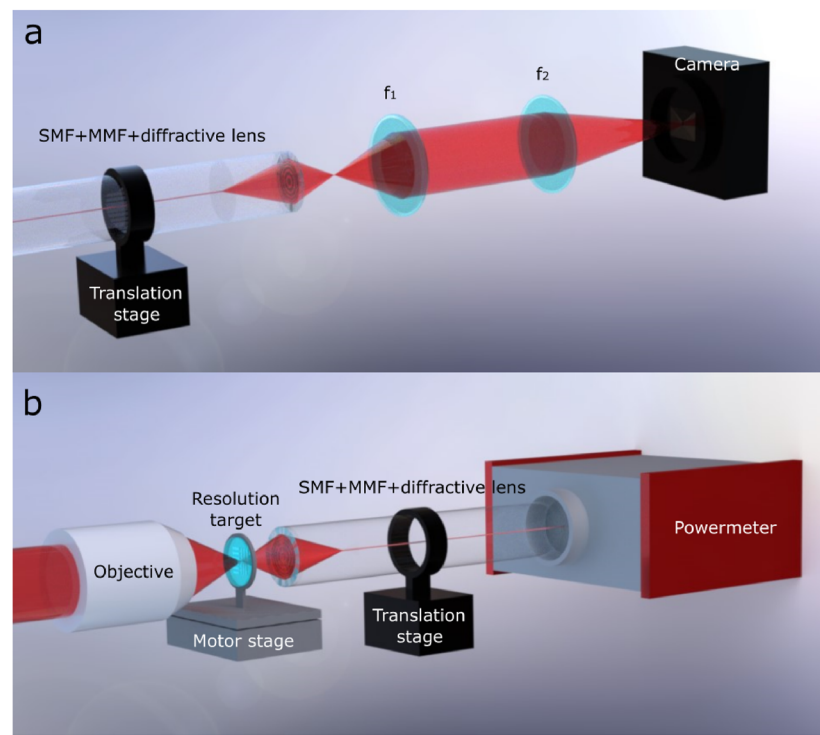


FIG. 5. Experimental optical setups for (a) output beam characterization and (b) imaging performance tests of the fiber devices. (a) The fiber patch cables are connected with a 660 nm laser source that illuminates the diffractive masks. A pair of lenses is used to form magnified focal spots onto a camera, and the depth-scan of the focal spot is accomplished via z-scan with a translation stage. (b) An objective (i.e., 10 \times and/or 20 \times) is used to focus the light onto a standardized resolution target, which is collected via the diffractive lenses into the fiber connected with a power meter to record light intensity. A motor stage is used to laterally translate the target, forming 2D images, and the depth scanning is performed similarly to (a) using z-translation.

(Thorlabs PM100USB). The resolution target is held and laterally translated via a motor stage to form 2D images, and the depth-scan is accomplished via a similar z-translation process. Using an illumination objective with a lower numerical aperture (NA) would increase the range for focused images and enhance the signal-to-noise ratio (due to higher coupling efficiency) to form images with higher quality [i.e., images in Fig. 3(i)]. However, using a high-NA objective in this specific experiment is preferable to properly examine the zone plate and axicon fibers for in-depth imaging capability.

Uniform and focused illuminations are both widely used for fiber imaging experiments. In this work, we choose the latter method, based on related work in the literature,²⁴ to emulate a real biomedical imaging scenario in which light is simultaneously focused and collected by the same fiber device in a reflection configuration. Furthermore, because the resolution target is a planar transmissive pattern, rather than, for example, a highly scattering tissue sample, collimated incident light is not highly divergent after passing through the sample. In this scenario, the fiber devices do not strongly exhibit their different depth-imaging abilities and behave more like “pin-hole” cameras with their small apertures not collecting out-of-focus light, regardless of the design of the lenses on their tips. Focused illumination is therefore required to properly examine the difference in imaging performance between the different designs.

APPENDIX B: IMAGE ANALYSIS

The resolution target imaging results may be different depending on the choice of illumination objectives numerical aperture (NA). A 20 \times objective (0.5 NA, 0.55 μm FWHM spot size in glass) is used in the experiment of the zone plate and axicon fibers because it is adequate to differentiate the depth-imaging abilities of them. Low-NA objectives (i.e., 5 \times , 0.15 NA and 10 \times , 0.3 NA) may give better coupling efficiency of light due to their closer match of NA to the fiber devices (bare fiber: 0.1 NA; zone plate fiber: 0.21 NA; axicon fiber: 0.08–0.18 NA) but reduce the ability to examine depth-imaging. We also note that the imaging experiment is achieved via a transmission measurement, the results of which can be differ from those obtained in reflection. As light illumination and collection are simultaneously achieved by the fiber device in a reflection measurement, its point-spread-function has a double influence on the retrieved images.

In order to quantify imaging performance, the recorded images are compared with an ideal in-focus “ground truth” image of the resolution target. Specifically, a 2D correlation measurement is used for the evaluation,

$$\text{corr} = \frac{\sum_x \sum_y (Ig_{xy} - \bar{Ig})(Ir_{xy} - \bar{Ir})}{\sqrt{(\sum_x \sum_y (Ig_{xy} - \bar{Ig})^2)(\sum_x \sum_y (Ir_{xy} - \bar{Ir})^2)}}, \quad (\text{B1})$$

where Ig_{xy} and Ir_{xy} are the values of each pixel in the ground-truth and fiber-retrieved images, respectively, and \bar{Ig} and \bar{Ir} are the mean values of the images.

We note that fringe contrast and edge response calculations are also widely used to analyze the imaging performance of resolution targets. However, beyond a certain distance from the fiber/lens (e.g., the bare-fiber images after 200 μm distance), it is difficult to

distinguish peaks and valleys, so the fringe contrast cannot be accurately estimated. Similarly, artifacts present in the background, due to additional speckle caused by the diffractive mask and sample imperfections, make edge response computations more susceptible to noise. The similarity approach is therefore more robust and gives the most reliable performance comparison.

APPENDIX C: DESIGN PRINCIPLE OF DEVICES

To demonstrate the versatility of our fabrication approach, we designed two types of diffractive lenses with different focal properties: a Fresnel zone plate and a diffractive axicon. The design principle of the Fresnel zone plate considers the optical path lengths (OPL) not only from the rings to the focal point but also from the starting point of the expanding source to the rings.⁵⁶ Specifically, the OPL of the ray from the m th order ring is m times half a wavelength more than that of the central ray,

$$nL_m + f_m = nL + f + m\lambda/2 \quad (m = 1, 2, \dots, N). \quad (\text{C1})$$

The radii of the rings R_m can be integrated into the equation using the Pythagorean theorem and solved in sequence [Fig. 6(a)]. The Fresnel zone plate is designed with a focal distance of 250 μm for 660 nm light, including accounting for the divergent incident wavefront caused by the fiber beam expander (a 750 μm long and 105 μm core-diameter multi-mode fiber segment fusion spliced onto the single-mode fiber²³) that enables filling of the lens aperture. For simplification, the multi-mode fiber (MMF) core is considered a homogeneous medium with a uniform refractive index, and the presence of the polymer encapsulation layer is neglected, assuming a zero-thickness binary mask on the homogeneous substrate surface. The diffractive lens can then be described by the following equation:

$$n\sqrt{L^2 + R_m^2} + \sqrt{f^2 + R_m^2} = nL + f + m\lambda/2 \quad (m = 1, 2, \dots, N), \quad (\text{C2})$$

where f is the focal length of the fiber device, L is the length of the beam expander, n is the refractive index of the MMF core (1.46), λ is the wavelength of light, R_m denotes the inner/outer edges of the annular rings at an integer m th order, and N is the total number of ring edges, which is 23 in this work.

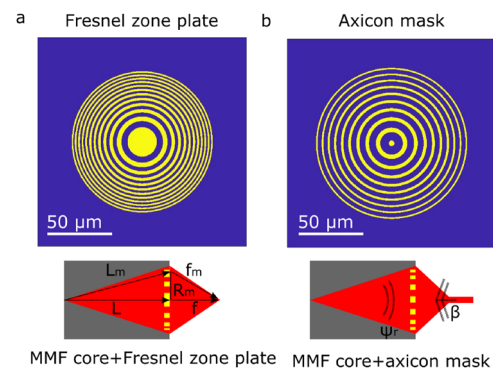


FIG. 6. Schematic illustration of the design principles for the (a) Fresnel zone plate and (b) axicon mask.

The axicon pattern is created via a binarization process similar to previously published works,^{57–59} which adjusts ring width and spacing to diffract input light into a Bessel beam. Specifically in this work, the designed pattern retrieves the desired phase of a conical-shaped wavefront from a spherical wave input (due again to the beam expander). In order to determine the correct profile of the amplitude grating, it is essential to know the phase profiles of the illumination beam and the output Bessel beam. The calculation of the illumination beam phase ψ_r at the MMF facet is illustrated in Fig. 6(b).

The electric field of the illumination beam at the MMF fiber core facet can be represented by the fundamental Gaussian function,⁶⁰

$$E_{r,z} = A_0 \frac{\omega_0}{\omega_z} e^{-\frac{r^2}{\omega_z^2}} e^{-i[k(z + \frac{r^2}{2R_z}) - \text{arctg} \frac{z}{z_0}]}, \quad (\text{C3})$$

where A_0 and ω_0 are the amplitude and beam radius at the waist ($z = 0$), respectively, ω_z and R_z are the beam radius and radius of wavefront curvature at distance z , respectively, and z_0 is the Rayleigh length. The relative phase profile at the MMF core facet can be directly derived from the imaginary term in Eq. (C3) by the calculation of wavefront curvature R_L at distance L ,

$$\psi_r = -\left[k\left(L + \frac{r^2}{2R_L}\right) - \text{arctg} \frac{L}{z_0} \right]. \quad (\text{C4})$$

The beam radius ω_L and wavefront curvature R_L at the facet are calculated via a complex-valued q parameter,⁶¹

$$\frac{1}{q_L} = \frac{1}{R_L} - i \frac{\lambda}{n\pi\omega_L^2}. \quad (\text{C5})$$

The input q-parameter at the waist q_0 can be easily obtained via the beam radius ($\omega_0 = 2 \mu\text{m}$ used in this work) and neglecting the real component ($R_0 = \infty$ at the waist). The output q-parameter at the facet q_L is calculated using the transformation law,

$$q_L = \frac{Aq_0 + B}{Cq_0 + D}, \quad (\text{C6})$$

where the transformation matrix is represented by the MMF length,

$$\begin{bmatrix} A & B \\ C & D \end{bmatrix} = \begin{bmatrix} 1 & L \\ 0 & 1 \end{bmatrix}. \quad (\text{C7})$$

Consequently, the beam radius ω_L and wavefront curvature R_L are obtained through solving the real and imaginary components of Eq. (C5), giving a solution to the input wavefront ψ_r .

The output phase of the conical wavefront ϕ_r desired for the Bessel beam is represented by the slope angle of the wavefront across the radial coordinates,⁵¹

$$\phi_r = -\frac{2\pi}{\lambda} r \sin \beta. \quad (\text{C8})$$

The slope angle is chosen to be 3.5° to set the length and position of the needle to a reasonable range for optical depth imaging (<1 mm, e.g., OCT) balanced with the practical fabrication requirement not to have too many or too few rings. Using geometrical optics, the needle

length may be estimated using formula (C9) with $\beta = 3.5^\circ$ and lens diameter $D = 108 \mu\text{m}$, giving a value of $l \approx 890 \mu\text{m}$, after which the light field begins to diverge significantly,

$$l = \frac{D}{2 \tan \beta}. \quad (\text{C9})$$

Next, the output phase profile and spherical wavefront correction term are combined to give a complex retardation

$$T_r = \exp [i(\phi_r - \psi_r)]. \quad (\text{C10})$$

This is then normalized through its real component,

$$T_{norm} = \frac{T_r - \min [\Re(T_r)]}{\max [\Re(T_r)] - \min [\Re(T_r)]}. \quad (\text{C11})$$

Finally, the complex-valued mask function is binarized using the formula

$$T(x, y) = \begin{cases} 1, & |T_{norm}| \geq 0.85, \\ 0, & |T_{norm}| < 0.85. \end{cases} \quad (\text{C12})$$

The generated pattern is illustrated in the schematic picture of Fig. 6(b). Compared to the Fresnel zone plate, the axicon mask consists of more evenly spaced rings, which are closer to a uniform annular diffraction grating.

APPENDIX D: DEVICE BEAM SIMULATION AND CHARACTERIZATION

It is essential to compare the performance of the output fields with the experimental measurement results. The diffractive lenses are simulated using Lumerical FDTD, assuming 100 nm thick gold masks (the same material and thickness used in the fabrication process) on homogeneous substrates (with the same refractive index as the MMF endcap core). In addition, the presence of the encapsulation layers (1.54 refractive index and 15 μm thickness, close to the fabricated thickness) is considered.

The simulation results in Fig. 7(a) show that the zone plate tightly focuses the light with intensity peaks at 245 and 70 μm depth-of-field. The lateral intensity profile in Fig. 7(b) further illustrates that light is shaped into a high-quality Gaussian focus with a 1.8 μm full width of half maximum (FWHM), which is also indicated by a close match between the simulation and the theoretical Airy function,

$$I = \left[\frac{2J_1(k \cdot NA \cdot r)}{k \cdot NA \cdot r} \right]^2, \quad (\text{D1})$$

where J_1 is a Bessel function of the first kind, and the numerical aperture (NA) of the zone plate can be directly calculated using the focal distance and the lens diameter (100 μm). The experimentally measured output light field from the zone plate fiber [via the setup in Fig. 6(a) from the main text] shows that the fabricated fiber device has output beam characteristics well-suited for fiber-imaging applications. This is illustrated in Fig. 7(c) by the tight focus at 235 μm with 100 μm depth-of-field, which closely matches the simulation result. The lateral intensity profiles in Fig. 7(d) further demonstrate that light is shaped into a high-quality Gaussian focus with a small

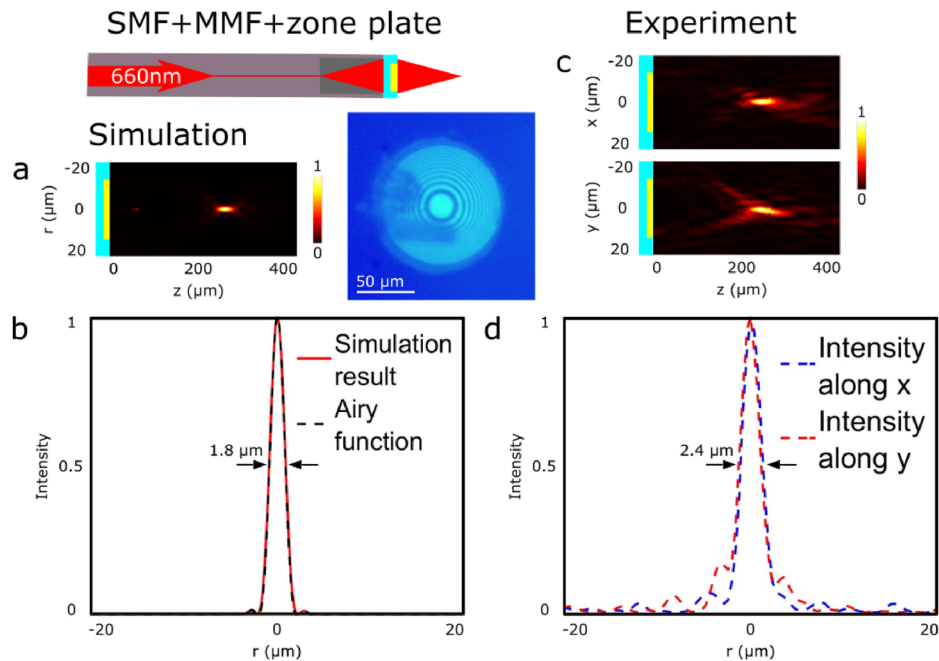


FIG. 7. Comparison between the numerically simulated (a) and (b) and experimentally measured (c) and (d) output field characteristics from the Fresnel zone plate fiber device shaping light into Gaussian foci. (a) and (c) show the cross-sectional intensity maps of the Gaussian foci. (b) and (d) show the line profiles of the Gaussian foci at the peak field-intensity planes, with $z = 245 \mu\text{m}$ in (a) and $z = 235 \mu\text{m}$ in (c), respectively. The result in (b) is overlaid with the theoretical Airy function. The microscope image of the fiber-attached zone plate is shown in the inset.

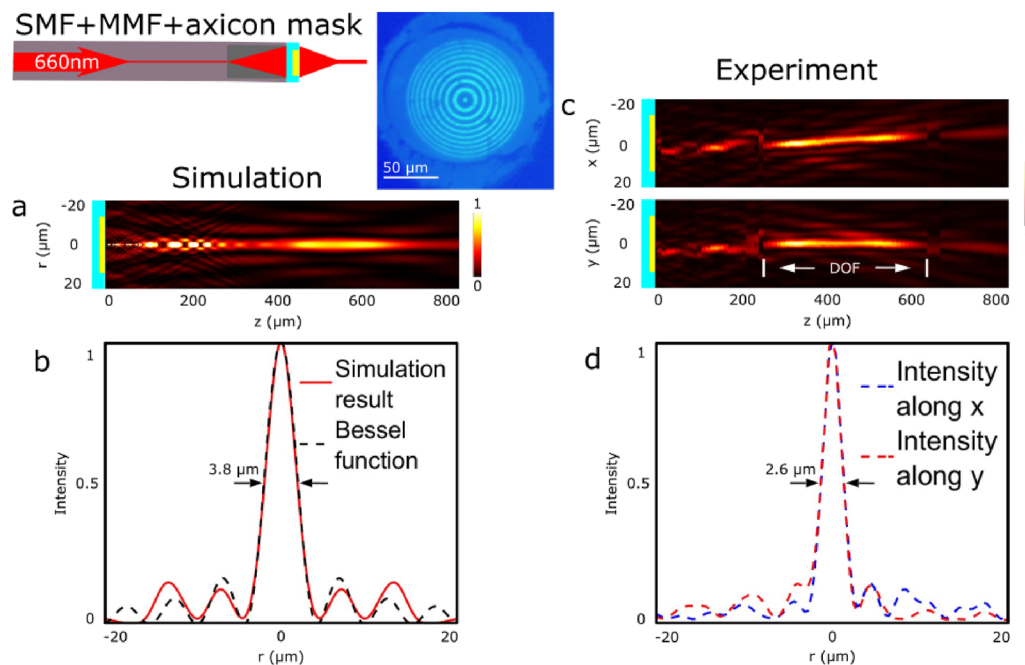


FIG. 8. Comparison between the numerically simulated (a) and (b) and experimentally measured (c) and (d) output field characteristics from the axicon fiber device shaping light into Bessel beams. (a) and (c) show the cross-sectional intensity maps of the Bessel beams. (b) and (d) show the line profiles of the Bessel beams at the peak field-intensity planes, with $z = 450 \mu\text{m}$ in (b) and $z = 320 \mu\text{m}$ in (d), respectively. The result in (b) is overlaid with the theoretical Bessel function. The microscope image of the fiber-attached axicon mask is shown in the inset.

degree of aberration and a $2.4 \mu\text{m}$ full width of half maximum (FWHM) spot size. The slight shift on the focal distance as well as the aberration on the focus can be attributed to mechanical distortion during the fabrication process and endcap length variation during the fiber-cleaving process.

In contrast to the zone plate fiber, the axicon fiber shapes light into a needle-like Bessel beam through the overlap between diffraction orders from the annular grating [Fig. 8(a)]. Due to the diffractive nature of the mask, the needle is not purely continuous and instead displays discrete high-order diffraction lobes at intermediate distances before the main lobe. The main lobe has a length of $400 \mu\text{m}$, and the light field diverges significantly after $800 \mu\text{m}$ distance from the fiber facet, closely matching the predictions from geometrical optics. The lateral intensity profile in Fig. 8(b) further illustrates that the field has a zero-order Bessel function distribution (as indicated by the pronounced side lobes) with a

$3.8 \mu\text{m}$ FWHM. The simulated result is also overlaid with the theoretical Bessel function,

$$I = [J_0(k \cdot NA \cdot r)]^2, \quad (\text{D2})$$

where J_0 is the Bessel function of the zeroth order and the NA is directly related to the designed slope angle of 3.5° mentioned in the device design section. The experimental measurement result in Fig. 8(c) illustrates that the output light maintains a needle-like shape for a $350 \mu\text{m}$ DOF, after which the light begins to diverge significantly at $650 \mu\text{m}$. The lateral intensity profile in Fig. 8(d) further proves that the field has a zero-order Bessel function distribution with a $2.6 \mu\text{m}$ FWHM spot size. The measured spot size and the needle range differ somewhat from the simulated results, and the measured properties suggest that they are produced by an axicon with an equivalent slope angle of 5° , slightly larger than designed.

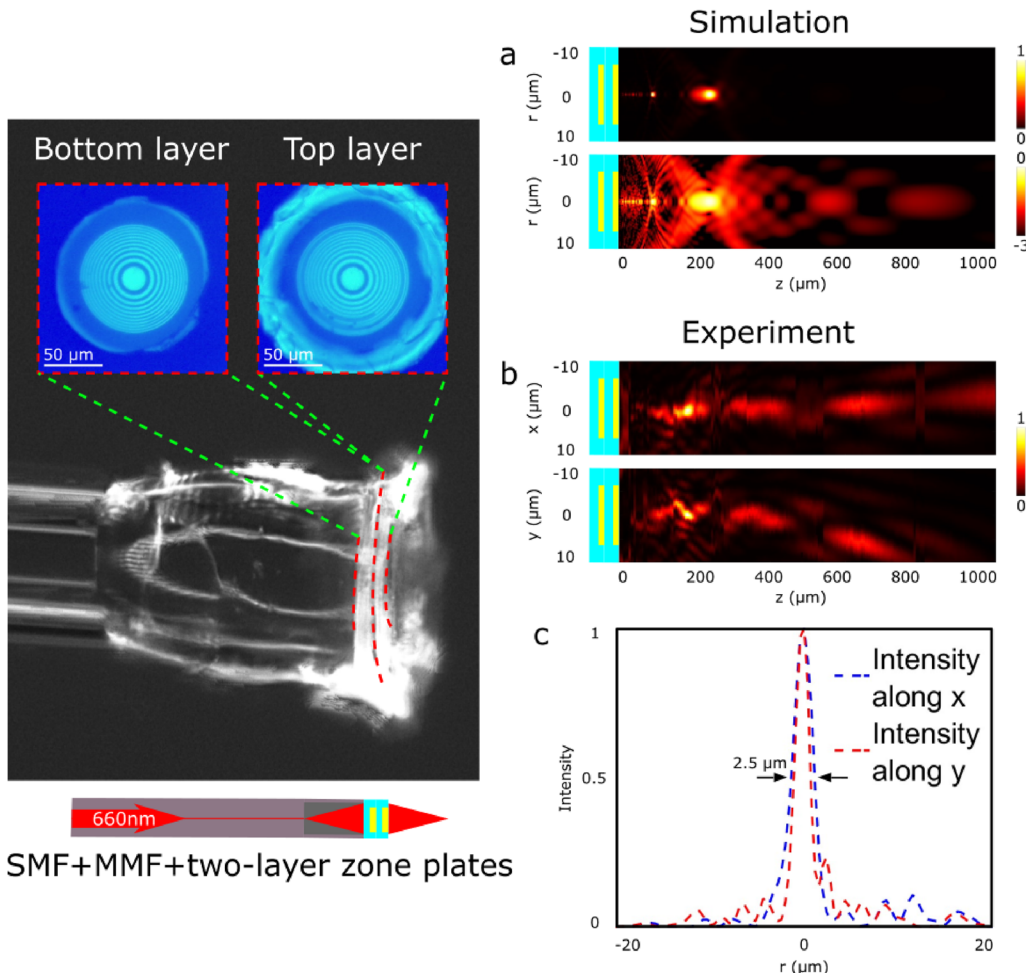


FIG. 9. Extension of our fabrication method to a two-layer zone plate on a fiber tip. (a) Numerical simulation of the output fields from a double-layer zone plate fiber device, showing the central-symmetrical foci in linear (top) and logarithmic (bottom) scales along radial coordinate r . (b) Experimental characterization of the output fields (linear scale only) from the fabricated double-layer fiber device, showing the cross-sectional intensity maps in two measurement planes, x - z (top) and y - z (bottom). (c) Line profiles of the focal spot at the field intensity-peak plane, $z = 180 \mu\text{m}$ in (b). The microscope images of the fiber device are shown in the inset.

This can be attributed to imperfections, such as slight distortion of the polymer layer during the pulling-up step from the hosting tape, resulting in deviations from the designed wavefront. Despite these imperfections, a tight lateral spot is maintained over a large depth-of-focus, making the axicon-fiber device a good candidate for depth imaging, such as fiber-based OCT.

We show the compatibility of our fabrication method with multi-layer structures by fabricating a double-layer Fresnel zone plate on a fiber. The device has two layers, each of which contains an identical zone plate, and is fabricated by performing the disk transfer and adhesion process twice in sequence [Figs. 2(b)–2(d) in the main text]. As shown in the inset of Fig. 9, minor imperfections can

be identified on the fabricated device, especially the top layer—one missing ring together with some damage to other rings during the detachment from the hosting tape. Such imperfections may affect the quality of the output field, leading to discrepancies between the experimental characterization and numerical simulation.

The simulation results show that the double-layer device focuses light at $240\ \mu\text{m}$ (slightly aberrated) with an equally strong side lobe at a closer distance to the fiber tip [Fig. 9(a), top panel]. The focal point does not have a significant shift compared with that of the single-layer zone plate device because the two diffractive masks have limited separation ($15\ \mu\text{m}$, the polymer thickness). This means that the two zone plates can be considered as one connected mask, giving

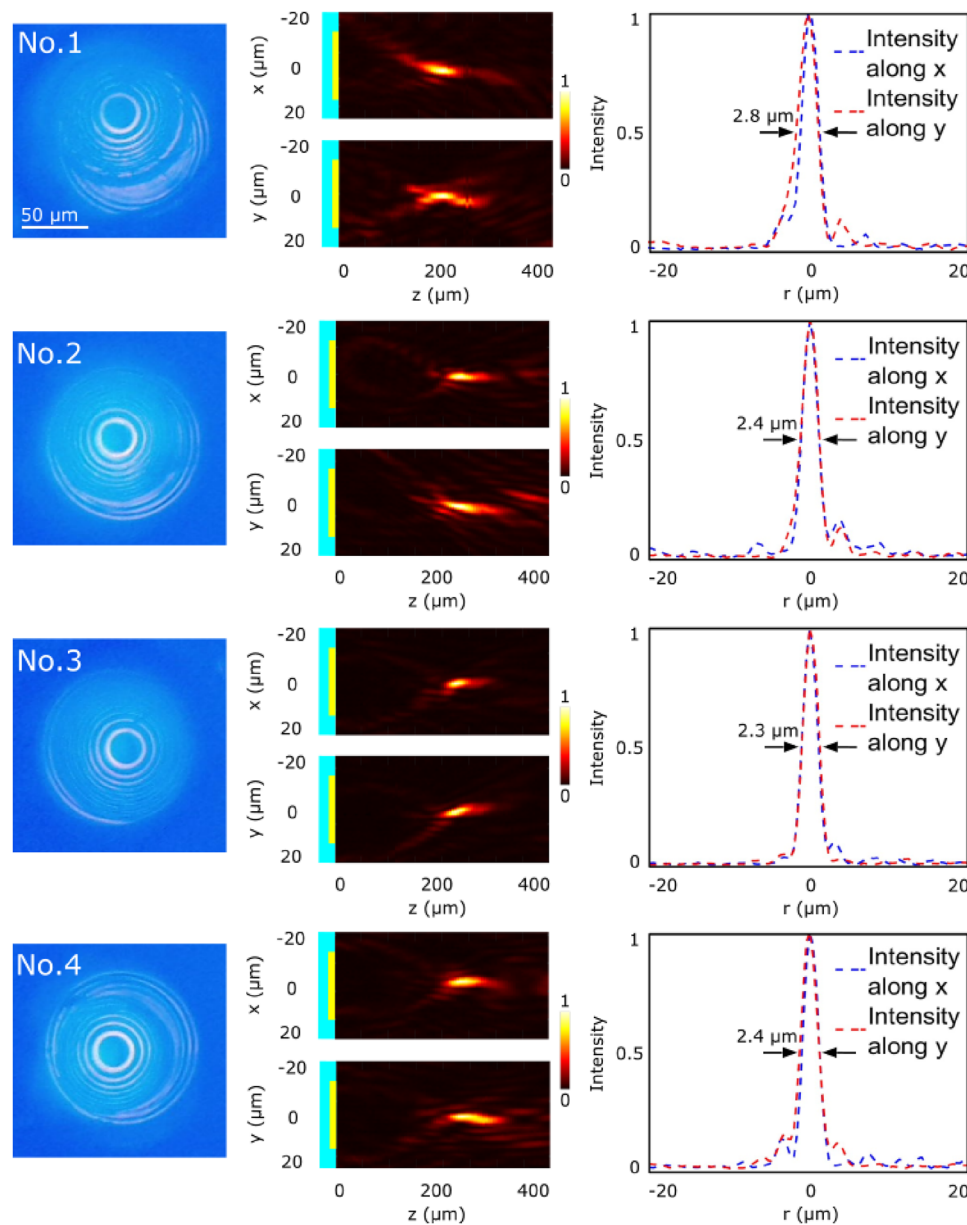


FIG. 10. Output beam characterization of four Fresnel zone plate fiber devices (lenses fabricated on SMF with an endcap) using the method shown in Fig. 2, demonstrating the fabrication reproducibility. The devices are illuminated with white light to visualize lens alignment with the fiber core. Cross-sectional intensity maps in the x-z and y-z planes, along with line profiles at the intensity peak plane, are shown for each device.

an insignificant positional shift on the main focusing lobe. However, due to the tiny perturbation on the input field by the second mask, an equally strong side lobe is created, and the intensity distribution in the main lobe is slightly asymmetrical. The perturbation may be further enlarged due to any imperfections present on the masks, such as our fabricated double-layer zone plates.

The experimentally characterized output field shows that the main focus lobe is shifted to $180\ \mu\text{m}$ ($60\ \mu\text{m}$ closer to the facet compared with the simulation result) and has noticeable additional lobes at larger distances [Fig. 9(b)]. The existence of these additional lobes is validated by the simulated field map in logarithmic scale [Fig. 9(a), bottom panel], but they are not properly suppressed on the fabricated device as the simulation [Fig. 9(a), top panel] due to fabrication imperfections. The slight distortions on the two encapsulated lenses (as well as little damage on the top lens) give rise to the focal point shift and the off-axis side lobes. Although the lateral focal spot has noticeable aberration [illustrated by the slightly asymmetrical spot shape and side diffraction rings in Fig. 9(c)], the central spot still has a clear Gaussian distribution, which indicates that the fiber device can have good imaging performance.

Four additional Fresnel zone plate fiber devices were fabricated using the methods illustrated in Fig. 2. The lenses in Fig. 10 have an alignment standard deviation of $6.8\ \mu\text{m}$ ($5.7\ \mu\text{m}$ if counting the other 4 lenses from Fig. 2). The output fields have standard deviations of $15.6\ \mu\text{m}$ in focal distances and $0.19\ \mu\text{m}$ in FWHM beam sizes, demonstrating the reproducibility of this fabrication method. Device No. 1 exhibits a more significant misalignment ($22\ \mu\text{m}$) compared to the other three devices ($5\text{--}7\ \mu\text{m}$ misalignment), resulting in a closer focal point and a larger beam size. This suggests that output beam aberration may be proportional to lens misalignment. However, a focal point can still form as long as a sufficient portion of the lens is illuminated, even in the presence of significant misalignment.

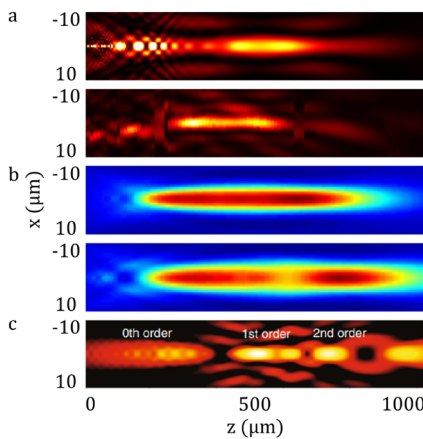


FIG. 11. Comparison between Bessel beam qualities from (a) this work (660 nm wavelength, simulation on the top and experimental measurement on the bottom), (b) the work from Lorensen *et al.*⁶² (820 nm), and (c) the work from Yin *et al.*⁶³ (800 nm). Panel (b) is adapted with permission from D. Lorensen *et al.*, Opt. Lett. **37**, 1616 (2012). Copyright 2012 Optica Publishing Group. Panel (c) is adapted from Yin *et al.*, Light: Sci. Appl. **8**, 104 (2019). Copyright 2019 Authors, licensed under a Creative Commons Attribution 4.0 license.

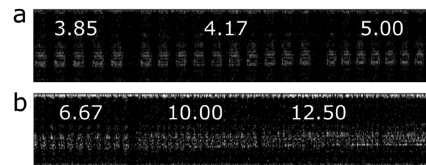


FIG. 12. OCT results on variable line gratings. The resolutions are (a) 3.85–5.00 lp/mm and (b) 6.67–12.50 lp/mm.

It is valuable to compare the Bessel beams generated in this work with those reported in the literature, as shown in Fig. 11. The needle beams produced by (b) Lorensen *et al.* and (c) Yin *et al.* exhibit greater depths ($\sim 1\ \text{mm}$) compared to (a) this work ($350\ \mu\text{m}$). This suggests that there is still room for improvement, particularly in extending the needle beam length. A preferred length range of 1–1.5 mm could be targeted, although it may come at the cost of an increased beam size.

To further characterize the OCT performance, we imaged variable line gratings (Thorlabs R1L3S6P). The resolved patterns in Fig. 12(a) have resolutions of 3.85, 4.17, and 5.00 lp/mm. In Fig. 12(b), the 12.50 lp/mm pattern begins to appear unresolved, with the least resolvable pattern having a resolution of 10.00 lp/mm, corresponding to $50\ \mu\text{m}$. As the single-mode fiber used in our device is optimized for 660 nm, it is significantly mismatched with the OCT system used for testing, which operates at 1310 nm, resulting in significant additional losses that can be reduced by using SMF-28 fibers. The resolution could be significantly improved by optimizing the device design for the OCT wavelength, enhancing back-reflected power for improved image construction.

REFERENCES

- D. Loterie, S. Farahi, I. Papadopoulos, A. Goy, D. Psaltis, and C. Moser, “Digital confocal microscopy through a multimode fiber,” *Opt. Express* **23**, 23845–23858 (2015).
- T. Čižmár and K. Dholakia, “Exploiting multimode waveguides for pure fibre-based imaging,” *Nat. Commun.* **3**, 1027 (2012).
- S. A. Vasquez-Lopez, R. Turcotte, V. Koren, M. Plöschner, Z. Padamsey, M. J. Booth, T. Čižmár, and N. J. Emptage, “Subcellular spatial resolution achieved for deep-brain imaging in vivo using a minimally invasive multimode fiber,” *Light: Sci. Appl.* **7**, 110–116 (2018).
- M. Gataric, G. S. D. Gordon, F. Renna, A. G. C. P. Ramos, M. P. Alcolea, and S. E. Bohndiek, “Reconstruction of optical vector-fields with applications in endoscopic imaging,” *IEEE Trans. Med. Imaging* **38**, 955–967 (2019).
- G. S. Gordon, M. Gataric, A. G. C. Ramos, R. Mouthaan, C. Williams, J. Yoon, T. D. Wilkinson, and S. E. Bohndiek, “Characterizing optical fiber transmission matrices using metasurface reflector stacks for lensless imaging without distal access,” *Phys. Rev. X* **9**, 041050 (2019).
- H. Pahlevaninezhad, M. Khorasaninejad, Y.-W. Huang, Z. Shi, L. P. Hariri, D. C. Adams, V. Ding, A. Zhu, C.-W. Qiu, F. Capasso, and M. J. Suter, “Nanooptic endoscope for high-resolution optical coherence tomography in vivo,” *Nat. Photonics* **12**, 540–547 (2018).
- W. Wang, G. Wang, J. Ma, L. Cheng, and B.-O. Guan, “Miniature all-fiber axicon probe with extended Bessel focus for optical coherence tomography,” *Opt. Express* **27**, 358–366 (2019).
- J. Li, S. Thiele, B. C. Quirk, R. W. Kirk, J. W. Verjans, E. Akers, C. A. Bursill, S. J. Nicholls, A. M. Herkommmer, H. Giessen, and R. A. McLaughlin, “Ultrathin monolithic 3D printed optical coherence tomography endoscopy for preclinical and clinical use,” *Light: Sci. Appl.* **9**, 124 (2020).

- ⁹J. Zhao, Y. Winetraub, L. Du, A. Van Vleck, K. Ichimura, C. Huang, S. Z. Aasi, K. Y. Sarin, and A. de la Zerda, "Flexible method for generating needle-shaped beams and its application in optical coherence tomography," *Optica* **9**, 859–867 (2022).
- ¹⁰M. Pahlevaninezhad, Y.-W. Huang, M. Pahlevani, B. Bouma, M. J. Suter, F. Capasso, and H. Pahlevaninezhad, "Metasurface-based bijective illumination collection imaging provides high-resolution tomography in three dimensions," *Nat. Photonics* **16**, 203–211 (2022).
- ¹¹R. Cao, J. Zhao, L. Li, L. Du, Y. Zhang, Y. Luo, L. Jiang, S. Davis, Q. Zhou, A. de la Zerda, and L. V. Wang, "Optical-resolution photoacoustic microscopy with a needle-shaped beam," *Nat. Photonics* **17**, 89–95 (2023).
- ¹²K. Sloyan, H. Melkonyan, and M. S. Dahlem, "Focused ion beam milling for prototyping 2D and 3D photonic structures," *Int. J. Adv. Des. Manuf. Technol.* **107**, 4469–4480 (2020).
- ¹³M. Principe, M. Consales, A. Micco, A. Crescittelli, G. Castaldi, E. Esposito, V. La Ferrara, A. Cutolo, V. Galdi, and A. Cusano, "Optical fiber meta-tips," *Light: Sci. Appl.* **6**, e16226 (2017).
- ¹⁴A. Xomalis, I. Demirtzioglou, E. Plum, Y. Jung, V. Nalla, C. Lacava, K. F. MacDonald, P. Petropoulos, D. J. Richardson, and N. I. Zheludev, "Fibre-optic metadevice for all-optical signal modulation based on coherent absorption," *Nat. Commun.* **9**, 182 (2018).
- ¹⁵M. Zeisberger, H. Schneidewind, U. Hübner, T. Wieduwilt, M. Plidschun, and M. A. Schmidt, "Plasmonic metalens-enhanced single-mode fibers: A pathway toward remote light focusing," *Adv. Photonics Res.* **2**, 2100100 (2021).
- ¹⁶A. Kuchmizhak, S. Gurbatov, A. Nepomniashchii, O. Vitrik, and Y. Kulchin, "High-quality fiber microaxicons fabricated by a modified chemical etching method for laser focusing and generation of Bessel-like beams," *Appl. Opt.* **53**, 937–943 (2014).
- ¹⁷K. Bachus, E. S. d. L. Filho, K. Włodarczyk, R. Oleschuk, Y. Messadeq, and H.-P. Loock, "Fabrication of axicon microlenses on capillaries and microstructured fibers by wet etching," *Opt. Express* **24**, 20346–20358 (2016).
- ¹⁸K. Vairagi, R. A. Minz, S. Kaur, D. Kumbhakar, S. Paul, U. Tiwari, R. K. Sinha, J. Fick, and S. K. Mondal, "Deep seated negative axicon in selective optical fiber tip and collimated Bessel beam," *IEEE Photonics Technol. Lett.* **29**, 786–789 (2017).
- ¹⁹T. Gissibl, S. Thiele, A. Herkommer, and H. Giessen, "Two-photon direct laser writing of ultracompat multi-lens objectives," *Nat. Photonics* **10**, 554–560 (2016).
- ²⁰I. V. A. K. Reddy, A. Bertoncini, and C. Liberale, "3D-printed fiber-based zeroth- and high-order Bessel beam generator," *Optica* **9**, 645–651 (2022).
- ²¹S. Lightman, O. Porat, G. Hurvitz, and R. Gvishi, "Vortex-Bessel beam generation by 3D direct printing of an integrated multi-optical element on a fiber tip," *Opt. Lett.* **47**, 5248–5251 (2022).
- ²²W. Hadibrata, H. Wei, S. Krishnaswamy, and K. Aydin, "Inverse design and 3D printing of a metasurface on an optical fiber tip for direct laser lithography," *Nano Lett.* **21**, 2422–2428 (2021).
- ²³M. Plidschun, H. Ren, J. Kim, R. Förster, S. A. Maier, and M. A. Schmidt, "Ultrahigh numerical aperture meta-fibre for flexible optical trapping," *Light: Sci. Appl.* **10**, 57 (2021).
- ²⁴H. Ren, J. Jang, C. Li, A. Aigner, M. Plidschun, J. Kim, J. Rho, M. A. Schmidt, and S. A. Maier, "An achromatic metafiber for focusing and imaging across the entire telecommunication range," *Nat. Commun.* **13**, 4183 (2022).
- ²⁵A. Asadollahbaik, S. Thiele, K. Weber, A. Kumar, J. Drozella, F. Sterl, A. M. Herkommer, H. Giessen, and J. Fick, "Highly efficient dual-fiber optical trapping with 3D printed diffractive Fresnel lenses," *ACS Photonics* **7**, 88–97 (2019).
- ²⁶G. Kostovski, U. Chinnasamy, S. Jayawardhana, P. R. Stoddart, and A. Mitchell, "Sub-15 nm optical fiber nanoimprint lithography: A parallel, self-aligned and portable approach," *Adv. Mater.* **23**, 531–535 (2011).
- ²⁷A. Koshelev, G. Calafiore, C. Piña-Hernandez, F. I. Allen, S. Dhuey, S. Sassolini, E. Wong, P. Lum, K. Munechika, and S. Cabrini, "High refractive index fresnel lens on a fiber fabricated by nanoimprint lithography for immersion applications," *Opt. Lett.* **41**, 3423–3426 (2016).
- ²⁸K. Huang, F. Qin, H. Liu, H. Ye, C.-W. Qiu, M. Hong, B. Luk'yanchuk, and J. Teng, "Planar diffractive lenses: Fundamentals, functionalities, and applications," *Adv. Mater.* **30**, 1704556 (2018).
- ²⁹A. Arbabi and A. Faraon, "Advances in optical metasurfaces," *Nat. Photonics* **17**, 16–25 (2023).
- ³⁰H.-T. Chen, A. J. Taylor, and N. Yu, "A review of metasurfaces: Physics and applications," *Rep. Prog. Phys.* **79**, 076401 (2016).
- ³¹S. M. Kamali, E. Arbabi, A. Arbabi, and A. Faraon, "A review of dielectric optical metasurfaces for wavefront control," *Nanophotonics* **7**, 1041–1068 (2018).
- ³²N. Yu and F. Capasso, "Optical metasurfaces and prospect of their applications including fiber optics," *J. Lightwave Technol.* **33**, 2344–2358 (2015).
- ³³Q. Zhao, W. Yuan, J. Qu, Z. Cheng, G.-D. Peng, and C. Yu, "Optical fiber-integrated metasurfaces: An emerging platform for multiple optical applications," *Nanomaterials* **12**, 793 (2022).
- ³⁴M. Kim, G. Yoo, B. Kim, Y. Song, and B. J. Lee, "Scalability enhancement in projection-based 3D printing through optical expansion," *Addit. Manuf.* **95**, 104511 (2024).
- ³⁵E. J. Smythe, M. D. Dickey, G. M. Whitesides, and F. Capasso, "A technique to transfer metallic nanoscale patterns to small and non-planar surfaces," *ACS Nano* **3**, 59–65 (2009).
- ³⁶M. Juhl, J. P. B. Mueller, and K. Leosson, "Metasurface polarimeter on optical fiber facet by nano-transfer to UV-curable hybrid polymer," *IEEE J. Sel. Top. Quantum Electron.* **25**, 1–7 (2019).
- ³⁷X. Sun, Z. Lei, H. Zhong, C. He, S. Liu, Q. Meng, Q. Liu, S. Chen, X. Kong, and T. Yang, "A quasi-3D fano resonance cavity on optical fiber end-facet for high signal-to-noise ratio dip-and-read surface plasmon sensing," *Light: Adv. Manuf.* **3**, 46 (2022).
- ³⁸L. Picelli, A. van Klinken, G. Lindgren, K. D. Hakkel, F. Pagliano, N. Fiaschi, I. Sersic-Vollenbroek, P. J. van Veldhoven, R. W. van der Heijden, and A. Fiore, "Scalable wafer-to-fiber transfer method for lab-on-fiber sensing," *Appl. Phys. Lett.* **117**, 151101 (2020).
- ³⁹X. Zhang, H. Cai, S. Daqiqeh Rezaei, D. Rosenmann, and D. Lopez, "A universal metasurface transfer technique for heterogeneous integration," *Nanophotonics* **12**, 1633–1642 (2023).
- ⁴⁰O. Avayu, E. Almeida, Y. Prior, and T. Ellenbogen, "Composite functional metasurfaces for multispectral achromatic optics," *Nat. Commun.* **8**, 14992 (2017).
- ⁴¹Y. Zhou, I. I. Kravchenko, H. Wang, J. R. Nolen, G. Gu, and J. Valentine, "Multilayer noninteracting dielectric metasurfaces for multiwavelength metaoptics," *Nano Lett.* **18**, 7529–7537 (2018).
- ⁴²D. J. Lipomi, R. V. Martinez, M. A. Kats, S. H. Kang, P. Kim, J. Aizenberg, F. Capasso, and G. M. Whitesides, "Patterning the tips of optical fibers with metallic nanostructures using nanoskiving," *Nano Lett.* **11**, 632–636 (2011).
- ⁴³M. Kim, N.-R. Park, A. Yu, J. T. Kim, M. Jeon, S.-W. Jeon, S.-W. Han, and M.-K. Kim, "Multilayer all-polymer metasurface stacked on optical fiber via sequential micro-punching process," *Nanophotonics* **12**, 2359 (2023).
- ⁴⁴P. Reader-Harris and A. Di Falco, "Nanoplasmonic filters for hollow core photonic crystal fibers," *ACS Photonics* **1**, 985–989 (2014).
- ⁴⁵A. Bertoncini and C. Liberale, "3d printed waveguides based on photonic crystal fiber designs for complex fiber-end photonic devices," *Optica* **7**, 1487–1494 (2020).
- ⁴⁶C.-F. Pan, H. Wang, H. Wang, P. N. S. Q. Ruan, S. Wredh, Y. Ke, J. Y. E. Chan, W. Zhang, C.-W. Qiu, and J. K. Yang, "3D-printed multilayer structures for high-numerical aperture achromatic metasurfaces," *Sci. Adv.* **9**, eadj9262 (2023).
- ⁴⁷C. Wang, Y.-X. Mao, Z. Tang, C. Fang, Y.-J. Yu, and B. Qi, "Numerical simulation of a gradient-index fibre probe and its properties of light propagation," *Chin. Phys. B* **20**, 114218 (2011).
- ⁴⁸Y. Karimi, H. Yang, J. Liu, B. h. Park, and M. Chamanzar, "Enhanced spectral-domain optical coherence tomography (SD-OCT) using in situ ultrasonic virtual tunable optical waveguides," *Opt. Express* **30**, 34256–34275 (2022).
- ⁴⁹R. Stephan, E. Scharf, K. Zolnacz, W. Urbanczyk, K. Hausmann, M. Ließmann, J. Gürler, T. Glosemeyer, J. Czarske, M. Steinke, and R. Kuschmierz, "Bendable fiber lens for minimally invasive endoscopy," *Laser Photonics Rev.* **19**, 2401757 (2025).
- ⁵⁰J. Shin, D. N. Tran, J. R. Stroud, S. Chin, T. D. Tran, and M. A. Foster, "A minimally invasive lens-free computational microendoscope," *Sci. Adv.* **5**, eaaw5595 (2019).

- ⁵¹ W. T. Chen, M. Khorasaninejad, A. Y. Zhu, J. Oh, R. C. Devlin, A. Zaidi, and F. Capasso, "Generation of wavelength-independent subwavelength Bessel beams using metasurfaces," *Light: Sci. Appl.* **6**, e16259 (2017).
- ⁵² M. Piccardo, M. de Oliveira, V. R. Policht, M. Russo, B. Ardini, M. Corti, G. Valentini, J. Vieira, C. Manzoni, G. Cerullo *et al.*, "Broadband control of topological-spectral correlations in space-time beams," *Nat. Photonics* **17**, 822–828 (2023).
- ⁵³ G. Yuan, E. T. F. Rogers, T. Roy, G. Adamo, Z. Shen, and N. I. Zheludev, "Planar super-oscillatory lens for sub-diffraction optical needles at violet wavelengths," *Sci. Rep.* **4**, 6333 (2014).
- ⁵⁴ F. Qin, K. Huang, J. Wu, J. Teng, C.-W. Qiu, and M. Hong, "A supercritical lens optical label-free microscopy: Sub-diffraction resolution and ultra-long working distance," *Adv. Mater.* **29**, 1602721 (2017).
- ⁵⁵ G. H. Yuan, E. T. Rogers, and N. I. Zheludev, "Achromatic super-oscillatory lenses with sub-wavelength focusing," *Light: Sci. Appl.* **6**, e17036 (2017).
- ⁵⁶ J. K. Kim, J. Kim, K. Oh, I.-B. Sohn, W. Shin, H. Y. Choi, and B. Lee, "Fabrication of micro Fresnel zone plate lens on a mode-expanded hybrid optical fiber using a femtosecond laser ablation system," *IEEE Photonics Technol. Lett.* **21**, 21–23 (2009).
- ⁵⁷ A. Vasara, J. Turunen, and A. T. Friberg, "Realization of general nondiffracting beams with computer-generated holograms," *J. Opt. Soc. Am. A* **6**, 1748–1754 (1989).
- ⁵⁸ A. Kołodziejczyk, S. Bará, Z. Jaroszewicz, and M. Sypek, "The light sword optical element—A new diffraction structure with extended depth of focus," *J. Mod. Opt.* **37**, 1283–1286 (1990).
- ⁵⁹ J. Sochacki, A. Kołodziejczyk, Z. Jaroszewicz, and S. Bará, "Nonparaxial design of generalized axicons," *Appl. Opt.* **31**, 5326–5330 (1992).
- ⁶⁰ H. Ye, Q. Sun, Z. Guo, Y. Hou, F. Wen, D. Yuan, F. Qin, and G. Zhou, "Theoretical realization of single-mode fiber integrated metalens for beam collimating," *Opt. Express* **29**, 27521–27529 (2021).
- ⁶¹ X. Zhou, Z. Chen, Z. Wang, and J. Hou, "Monolithic fiber end cap collimator for high-power free-space fiber–fiber coupling," *Appl. Opt.* **55**, 4001–4004 (2016).
- ⁶² D. Loreser, X. Yang, and D. D. Sampson, "Ultrathin fiber probes with extended depth of focus for optical coherence tomography," *Opt. Lett.* **37**, 1616–1618 (2012).
- ⁶³ B. Yin, Z. Piao, K. Nishimiya, C. Hyun, J. A. Gardecki, A. Mauskapf, F. A. Jaffer, and G. J. Tearney, "3D cellular-resolution imaging in arteries using few-mode interferometry," *Light: Sci. Appl.* **8**, 104 (2019).